Transport Modeling Of Locally Photogenerated Excitons In Halide Perovskites

Kuen Wai Tang,[†] Senlei Li,[‡] Spencer Weeden,[¶] Ziyi Song,[‡] Luke McClintock,[‡] Rui Xiao,[‡] R. Tugrul Senger,[§] and Dong Yu[‡]

[†]*Department of Physics and Astronomy, University of California–Davis, One Shields Avenue, Davis, CA 95616*

[‡]*Department of Physics and Astronomy, University of California-Davis, One Shields Avenue, Davis, CA 95616*

[¶]*Department of Physics, Carleton College, Sayles Hill Campus Center, North College Street, Northfield, MN 55057*

[§]*Department of Physics, Izmir Institute of Technology, 35430 Izmir, Turkey*

Abstract

Excitons have fundamental impacts on optoelectronic properties in semiconductors. Halide perovskites, with long carrier lifetimes and ionic crystal structures, may support highly mobile excitons because the dipolar nature of excitons suppresses phonon scattering. Inspired by recent experimental progress, we perform device modeling to rigorously analyze the exciton formation and transport in methylammonium lead triiodide under local photoexcitation, by using a finite element method. Mobile excitons, coexisting with free carriers, can dominate the photocurrent generation at low temperatures. The simulation results are in excellent agreement with the experimentally observe
fies tha
family

Graphi

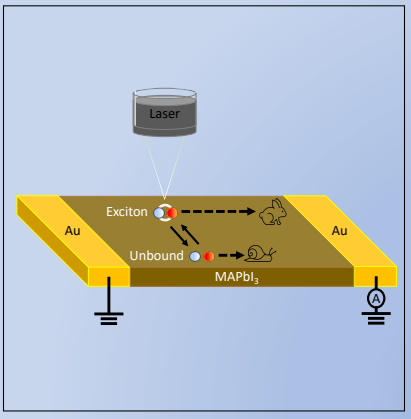

Carrier diffusion in halide perovskites can be significantly enhanced by efficient transport of excitons.

Excitons, electron-hole pairs bound by Coulomb interaction, not only greatly influence the optical properties of semiconducting materials by creating resonant optical absorption, but also play a crucial role in the electronic properties such as how photoexcited carriers transport in the materials. Furthermore, the fundamental research on excitons has revealed fascinating and rich physics. Excitons can form more complicated quasi-particles such as trions, biexcitons,[1,2] exciton polarons,[3] and exciton polaritons.[4] Excitons may undergo a gas-liquid phase transition[5] and condense into an electronic insulator or a superfluidic quantum state.[6,7] How excitons interact with free carriers and phonons is essential to understanding these exotic behaviors. For example, in wide-bandgap semiconductors with low dielectric constants, excitons heavily dressed by phonons can be immobilized by a self-trapping mechanism, such as in the case of metal halides and one-dimensional (1D) hybrid halide perovskites.[8,9] However, in inorganic semiconductors with larger dielectric constants, electric field screening can result in highly mobile excitons, exhibiting mobilities as high as 2×10^6 cm^2/Vs at 1.5 K in Si.[10]

Hybrid halide perovskites show unique properties that facilitate the unprecedented rapid development in optoelectronic applications such as solar cells and light emitting devices. Halide perovskites have been shown to have a soft lattice with Young's moduli approximately 10 times lower than common inorganic semiconductors.[11] As a result of the highly polarizable lattice, a charge carrier can effectively form a large polaron with a diameter much larger than the unit cell size.[12] Large polarons in halide perovskites may account for the unique optoelectronic properties of the materials, including electric field screening, defect tolerance, slow hot carrier cooling, and moderate charge carrier mobility.[13,14] Analogous to charged (electron or hole) polarons, excitons may interact with the crystal lattice and form polaronic excitons. The phonon-scattering of exciton polarons is fundamentally different from charged polarons and is poorly understood. The carrier scattering is expected to be dominated by longitudinal optical (LO) phonons in halide perovskites.[15]

We recently proposed that the phonon-scattering rate of excitons can be significantly suppressed compared to free carriers and charged polarons, since the electric field created by

a dipole is shorter-ranged than the monopolar field.[16] Briefly, the interaction of an exciton with LO phonons can be modeled through its induced dipole moment, expressed similar to the polarizability of a hydrogen atom, $\alpha = 9a_{ex}^3/2$, where a_{ex} is the exciton Bohr radius.[17] The interplay between the excitonic and polaronic effects in halide perovskites is highly elaborate and it has been a subject of debate in the literature in various forms. Halide perovskites are highly polar materials with significantly different values of optical and static dielectric constants, and they have lower phonon energies due to their softness. These two properties combine to lead to high Fröhlich coupling constants for the charge-phonon interactions. Therefore, the simple hydrogenic model of excitons does not apply well in these materials. To characterize the excitons we use exciton size and binding energy values as calculated using an effective interaction potential model for polaronic excitons.[18,19] In this model, the scattering rate of an exciton from LO phonons is reduced by a factor of $\gamma = (\frac{9a_{ex}^3 R_h}{2\varepsilon_\infty R_{ex}^4})^2$ compared to a hole. Here, R_h and R_{ex} are the hole and exciton polaron radii, respectively, where the polaron radius of a quasi particle of mass m interacting with LO phonons is given by $R = \sqrt{\frac{\hbar}{2m\omega_{LO}}}$. We have estimated that $\gamma \approx 10^{-3}$, indicating exciton mobility is significantly higher than that of free carriers or charged polarons.[16]

This theoretical prediction is supported by our experimental observation of strong temperature dependence of photogenerated carrier diffusion in single-crystal methylammonium lead triiodide ($MAPbI_3$) microstuctures, by scanning photocurrent microscopy (SPCM).[16] Carrier diffusion lengths were found to increase much more rapidly than expected from phonon scattering of charged polarons as temperature decreased. Instead, the experimental results can be understood by the exponentially increased fraction of highly mobile excitons at low temperature. Furthermore, carrier diffusion lengths were found to increase by a factor of 8 with increasing majority carrier (electron) concentration under gate voltage (V_G). This is also consistent with the exciton model, as the higher carrier concentration increases the probability of exciton formation,[20] leading to a larger exciton fraction and hence higher effective mobility.

Here, inspired by the previous experimental work, we perform device modeling and numerical simulations to rigorously analyze the exciton formation and transport in $MAPbI_3$ microstructures under local photoexcitation. The simulation results agree well with our experimental observations including temperature and gate dependent photocurrent decay lengths. A similar approach[21] has been applied to simulate the excitonic effects in conducting polymer solar cells, but excitons were treated as immobile particles. In this letter, we instead consider that excitons are significantly more mobile than free carriers. Another major difference is that the device geometry examined in the previous work was a solar cell under uniform illumination, while we consider a point photoexcitation as used in SPCM. SPCM is a powerful experimental technique that provides spatially resolved photocurrent mapping and insights on carrier transport.[22–24] In particular, this method has been recently applied to extract carrier diffusion length, a crucial optoelectronic parameter in halide perovskites.[16,25–27] However, these previous SPCM efforts have only considered free carriers, ignoring the contribution of excitons. We show that excitons can actually dictate the photocurrent distributions at low temperature.

We consider three types of coexisting particles in the material under light illumination: free electron, free hole, and exciton. To be clear, by "free" we mean the electron and hole are not bound into an exciton. But they may still be dressed by phonons, resulting in reduced mobilities. A free electron and a free hole are bound into an exciton at a rate described by Langevin recombination (k_r), which assumes an exciton forms once an electron and a hole move within their joint capture radius,[28]

$$k_r = \frac{\mu e}{\epsilon_r \epsilon_0} \tag{1}$$

where $\mu = \mu_n + \mu_p$ is the sum of electron and hole mobilities and ϵ_r is the dielectric constant. An exciton can also dissociate into a free electron and a free hole at a rate that depends on the local electric field E,

$$k_d(E) = k_r K(E) \tag{2}$$

At $E = 0$, the equilibrium constant of exciton dissociation $K(0)$ is given by,[29]

$$K(0) = \frac{3}{4\pi a_{ex}^3} e^{-E_b/k_B T} \tag{3}$$

where a_{ex} is the exciton size and $E_b = \frac{e^2}{4\pi\epsilon_r\epsilon_0 a}$ is the exciton binding energy. In the presence of electric field, excitons dissociate at a higher rate given by,[28]

$$K(E)/K(0) = \frac{J_1(2\sqrt{-2b})}{\sqrt{-2b}} \tag{4}$$

where J_1 is the Bessel function of order one and $b = \frac{e^3 E}{8\pi\epsilon_r\epsilon_0 k_B^2 T^2}$.

As depicted in Figure 1(a), photogenerated excitons coexist with free charge carriers via the above formation and dissociation processes. Both excitons and free carriers can recombine to the ground state, as well as drift and diffuse to other locations. To find the densities of free electrons (n), free holes (p), and excitons (n_{ex}), one needs to solve the electrostatic and continuity equations,

$$\nabla \cdot \vec{E} = e(p + N_d - n - N_a)/\epsilon_r\epsilon_0 \tag{5}$$

$$\frac{dn}{dt} = k_d(E) n_{ex} - k_r np - R_{SRH} - \nabla \cdot \vec{J_n} \tag{6}$$

$$\frac{dp}{dt} = k_d(E) n_{ex} - k_r np - R_{SRH} - \nabla \cdot \vec{J_p} \tag{7}$$

$$\frac{dn_{ex}}{dt} = G_{ex} + k_r np - k_d(E) n_{ex} - n_{ex}/\tau_{ex} - \nabla \cdot \vec{J_{ex}} \tag{8}$$

where N_a is the acceptor concentration, N_d is the donor concentration, G_{ex} is the photoex-

citation rate, and τ_{ex} is the lifetime of excitons. G_{ex} in Equation 8 is set to initially generate excitons. We note that the simulation results do not change if photoexcitation initially generates free carriers. The simulated photocurrent distributions and photocurrent decay lengths remain the same if G_{ex} is moved to Equations 6 and 7 as shown in Figure S1b in the Supporting Information. This is because the excitons and free carriers quickly reach a balance through the fast pairing and dissociation process, regardless of whether excitons or free carriers are generated initially. Furthermore, higher order terms such as Auger recombination may have impacts on the diffusion length as observed in WS_2 monolayers.[30] However, we do not consider that in this work as we used relatively low laser power and did not observe extension of diffusion lengths at higher laser power in our previous experiments.[16] At high laser intensity, the bimolecular recombination may lead to a reduced effective carrier lifetime. For simplicity, we also ignore this effect. We assume that free carriers recombine through the Shockley-Read-Hall process at a rate R_{SRH},

$$R_{SRH} = \frac{np - {n_i}^2}{\tau_p(n + n_i) + \tau_n(p + n_i)} \tag{9}$$

$\vec{J_n}$, $\vec{J_p}$, $\vec{J_{ex}}$ are number (not charge) current densities of electrons, holes, and excitons, respectively. Each current density has both diffusion and drift components. Explicitly, we have,

$$\vec{J_n} = -\mu_n n\vec{E} - \mu_n k_B T \nabla n/e \tag{10}$$

$$\vec{J_p} = \mu_p p\vec{E} - \mu_p k_B T \nabla p/e \tag{11}$$

$$\vec{J_{ex}} = -\mu_{ex} k_B T \nabla n_{ex}/e \tag{12}$$

where μ_n, μ_p, μ_{ex} are the mobilities of electrons, holes, and excitons, respectively. We

assume Einstein relation is held in all three cases (for example, the diffusivity of excitons is $D_{ex} = \mu_{ex} k_B T/e$). The drift term in exciton current is absent because excitons are charge neutral. We ignore photoinduced thermoelectric current as the observed photocurrent is much larger than that expected from such an effect,[16] confirmed by previous simulation work.[23,24]

The above equations can only be solved analytically by making some extreme assumptions. Though these assumptions are perhaps over-simplified, the analytic solutions can help understand the physical mechanisms. We will consider three different assumptions below.

First, we consider that the material is under homogeneous photoexcitation. In this case, free carriers and excitons are uniformly distributed so all currents are zero. In addition, the carrier pairing rate k_r is estimated to be 10^{-5} cm^3 s^{-1} using a mobility of 100 cm^2/Vs, corresponding to a pairing time $\tau_{pair} = \frac{1}{k_r n}$ of a few ps for $n = 10^{16}$ cm^{-3}. This is much faster than the carrier recombination with a timescale of 100 ns. Thus, we can also drop the n_{ex}/τ_{ex} term in Equation 8. In the absence of electric field, this then becomes an equilibrium equation,

$$np/n_{ex} = K(0) = \frac{3}{4\pi a_{ex}^3} e^{-E_b/k_B T} \tag{13}$$

This equation describes the ratio of the free carrier densities over the exciton density in pseudo-equilibrium. We shall see that this relation is held quite precisely even under inhomogeneous photoexcitation, as confirmed by the simulation results shown later. We also note that the above equation is similar in form to the Saha-Langmuir equation,[20,31] with the thermal deBroglie wavelength ($\lambda = h/\sqrt{2\pi m_{ex}^* k_B T}$, where $m_{ex}^* = m_e m_h/(m_e + m_h)$ is the effective mass of an exciton) replaced by the exciton size a_{ex}. Both the Saha-Langmuir equation and equation 13 have been used to relate the exciton and free carrier densities in equilibrium.[20,21,28,32] Here we choose to use equation 13. As λ and a_{ex} are on the same order of magnitude, this choice is not expected to change our qualitative conclusions. More exactly in $MAPbI_3$, λ is estimated to be 5 times larger than a_{ex} at 300 K and 10 times larger at

50 K. As a result, Saha model predicts a higher exciton fraction than that predicted from the Langevin model. Understanding this interesting discrepancy requires further theoretical and experimental work and is beyond the scope of this work.

Second, we consider a point photoexcitation source, but assume that exciton density is negligibly small when $E_b << k_BT$. In this case, Equations 6 and 7 are reduced to the continuity equations for free carriers alone. One can show[22] that the photocurrent decays exponentially as the point photoexcitation is moved away from the contact ($I = I_0 e^{-x/L_d}$), with a decay length that equals to the minority carrier diffusion length, for example, $L_d = \sqrt{D_p \tau_p}$ in n-type semiconductors.

Third, a more interesting assumption is that excitons are much more mobile than free carriers ($\mu_n << \mu_{ex}$ and $\mu_p << \mu_{ex}$) as indicated in our previous work.[16] In this extreme case, we can ignore the drift and diffusion of free carriers ($J_n = J_p = 0$). To simplify the discussion, we can assume the material is n-type and hence $R_{SRH} = p/\tau_p$ at low photoexcitation intensity. Considering a steady state where carrier concentration is time independent, summing Equations 7 and 8 yields,

$$\nabla \cdot \vec{J}_{ex} = G_{ex} - n_{ex}/\tau_{ex} - p/\tau_p \tag{14}$$

In the region outside the photoexcitation point, $G_{ex} = 0$ and the above equation in 1D becomes,

$$D_{ex} \frac{d^2 n_{ex}}{dx^2} = n_{ex}/\tau_{ex} + p/\tau_p \tag{15}$$

If we can further assume free carriers and excitons reach a dynamic balance at any position, we can use Equation 13 to eliminate p. In addition, $n \approx N_d$ is expected to be uniform under low photoexcitation in n-type devices, so we have,

$$D_{ex} \frac{d^2 n_{ex}}{dx^2} = n_{ex}[1/\tau_{ex} + K(0)/N_d \tau_p] = n_{ex}/\tau_{eff} \tag{16}$$

where τ_{eff} is the effective lifetime. The solution to this equation is a simple exponential distribution of exciton concentration, indicating that photocurrent exponentially decays with a decay length that is determined by the exciton diffusion coefficient and a hybrid effective lifetime,

$$L_d = \sqrt{D_{ex}\tau_{eff}} = \sqrt{\frac{D_{ex}}{1/\tau_{ex} + K(0)/N_d\tau_p}} \tag{17}$$

We carry out numerical simulation by a finite element method to more rigorously solve the differential equations. We consider a device configuration similar to that in our previous experimental work,[16] where a microribbon of $MAPbI_3$ is in contact with two Au electrodes. A Gaussian distribution ($G_{ex} = G_0 \exp\left[-\frac{(x-x_0)^2}{2\sigma^2}\right]$) is assumed for the photoexcitation induced by the focused laser beam, where G_0 is the maximum carrier generation rate, x_0 is the laser center position, and σ is the Gaussian width. Because the CW laser scans slowly (a line scan takes about 1 second), a steady state can be assumed. We focus on devices with Schottky junctions at the $MAPbI_3$ and Au interface, as experimentally shown.[16,25] The typical size of the microribbon is tens of μm's long, 1 μm thick, and 1 μm wide. As the longitudinal dimension is much larger than the lateral dimension in these microstructures, the three dimensional (3D) charge transport can be simulated by 1D equations. The photoexcitation absorbed near the top of the microribbon (typically within the optical absorption depth of tens of nm's) and the bottom gate may create inhomogeneous carrier distributions. However, even with such inhomogeneity, the 3D carrier transport can be simplified into 1D, because the carriers flow parallel to the channel in most of the transport path in the device channel as previously shown.[23]

The device configuration used in the simulation was slightly different from our previous experimental setup[16] because 1D simulation does not allow for extraction of the photocurrent distributions outside the source-drain channel. Instead, the device was composed of a 1D channel between source and drain contacts as shown in Figure 1b, where we can still extract the carrier diffusion lengths from the photocurrent decay inside the channel to compare with

our previous experimental results. To ensure the diffusion nature, a zero source-drain bias was used in the simulation. A relatively large, 600-μm channel was used for the accurate extraction of the long photocurrent decay length at low temperature.[24]

All physical parameters used in the simulation were chosen to represent the realistic experimental conditions and the $MAPbI_3$ microribbon properties.[16] We assumed an n-type channel with a donor concentration of $N_d = 5 \times 10^{16}$ cm^{-3} by default. The gate effect was considered by directly changing N_d. Schottky junctions with a barrier height $q\Phi_B = 0.35$ eV were used for both contacts, similar to that in real devices. At the metal contacts, we assume that the recombination occurs very fast, such that an equilibrium is reached: (1) both the quasi-Fermi levels of free electrons and holes are equal to the work function of the metal, and (2) free carriers and excitons reach equilibrium, i.e., $np/n_{ex} = K(E_m)$, where E_m is the electric field at the metal contact and is estimated from the abrupt Schottky junction equation. Both measured and calculated values of exciton binding energies in $MAPbI_3$ have been reported in a broad range from a few meV to over 50 meV.[33] However, it is largely agreed that the binding energy of excitons is considerably larger in the low-temperature crystal phase. The exciton binding energy values used in our simulation were chosen to be 10 meV for the tetragonal phase and 20-30 meV for the orthorhombic phase below $T_c = 160$ K, consistent with the typical values in previous reports.[34] The justification of values for dielectric constants and exciton size can be found in a reference.[16] We set exciton mobility to be about 300 times of that for free carriers and their values were chosen to match our experimental results. We chose temperature dependent mobilities for both free carriers and excitons, $\mu \sim T^{-3/2}$, assuming phonon scattering is dominating.[10,35] Lifetimes of free carriers and excitons were chosen to have a similar power law dependence, $\tau \sim T^{-3/2}$.[36] We note that the simulation results are robust against the details of the power law dependence of mobilities and lifetimes, since the dominating factor governing the temperature dependent diffusion length is the exciton fraction which exponentially depends on T. The simulated diffusion length is similar when using a T independent lifetime (Figure S2 in the Supporting

Information). Simulation parameters are listed in Table 1.

Python with SciPy library was used as a differential equation solver. Non-uniform mesh sizes were used, with a high resolution 3-nm mesh size near the metal-semiconductor junctions and the laser injection position, and gradually increasing mesh sizes to a few hundred nm's at places where carrier concentrations slowly varied. We confirmed that simulations using finer mesh did not show notable changes. We further cross-checked the Python simulation results with COMSOL Multiphysics, a commercial finite element solver. The two methods generated highly consistent results as shown in Figure S1c in the Supporting Information. We chose to mainly use Python because of its flexibility.

Table 1: Simulation parameters.

symbol	physical meaning	value
E_g	bandgap	1.61 eV
N_d	donor concentration	5×10^{16} cm^{-3}
N_A	acceptor concentration	0
$q\Phi_B$	Schottky barrier height	0.35 eV
ε_r	dielectric constant	30.4 ($T \geq 160K$) 25.7 ($T \leq 160K$)
a_{ex}	exciton size	3.37 nm ($T \geq 160K$) 2.95 nm ($T \leq 160K$)
E_b	exciton binding energy	10 meV ($T \geq 160K$) 20 or 30 meV ($T \leq 160K$)
m_e	electron effective mass	0.19 m_0
m_h	hole effective mass	0.23 m_0
μ_n	electron mobility	$96.6 \times (\frac{300}{T})^{\frac{3}{2}}$ cm^2/Vs
μ_p	hole mobility	$96.6 \times (\frac{300}{T})^{\frac{3}{2}}$ cm^2/Vs
μ_{ex}	exciton mobility	$27482 \times (\frac{300}{T})^{\frac{3}{2}}$ cm^2/Vs
τ_n	electron lifetime	$100 \times (\frac{300}{T})^{\frac{3}{2}}$ ns
τ_p	hole lifetime	$100 \times (\frac{300}{T})^{\frac{3}{2}}$ ns
τ_{ex}	exciton lifetime	$1000 \times (\frac{300}{T})^{\frac{3}{2}}$ ns
L	channel length	600 μm
A_z	cross-section area	0.4 μm^2
λ	laser wavelength	532 nm
σ	laser beam width	200 nm

Spatial distributions of free charge carriers and excitons. We first present the

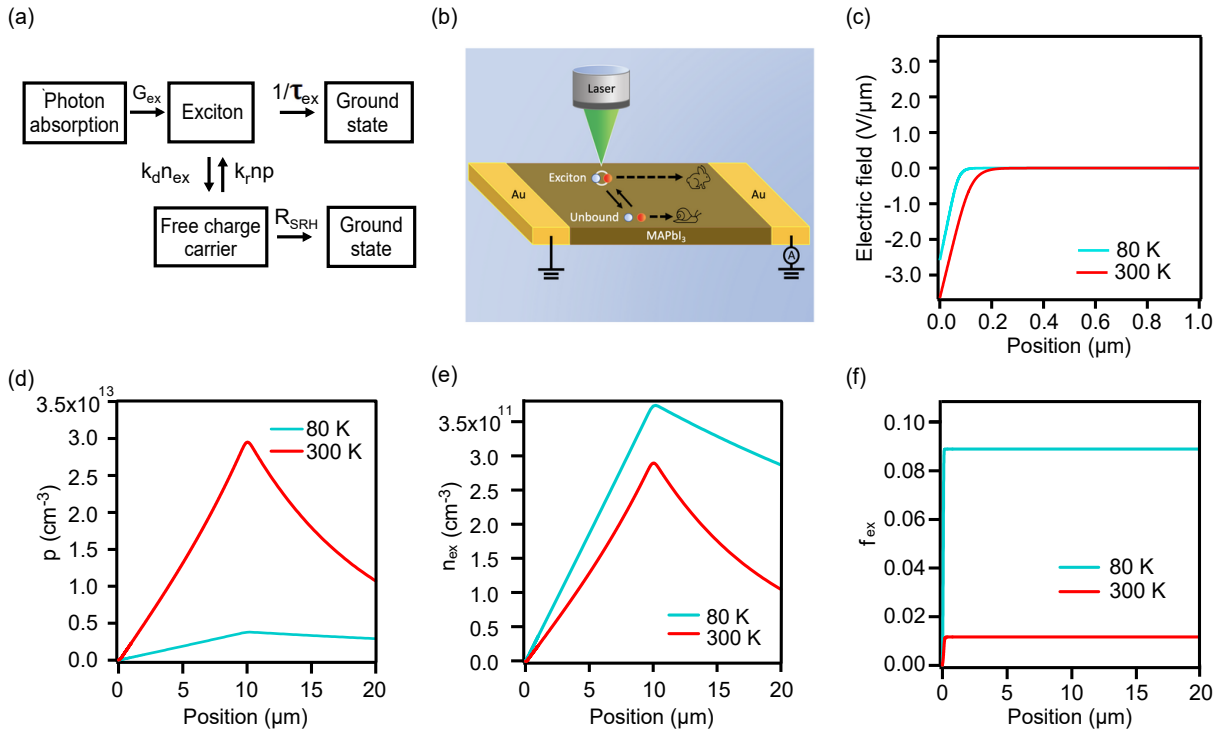

Figure 1: Simulated distributions of electric field, free carriers and excitons, under point excitation at $x = 10\ \mu m$ with a power of $P = 1$ nW, and $V_{sd} = 0\ V$ in a $MAPbI_3$ nanoribbon device. (a) Diagram showing the generation, pairing/dissociation, and recombination processes of coexisting excitons and free carriers. (b) Schematic drawing of device configuration under a focused laser and the generation and transport of excitons and free carriers. (c-f) Distribution of electric field (c), free hole density (d), exciton density (e), and exciton fraction (f) at 80 and 300 K respectively. E_b is set to be 10 meV at 300 K and 20 meV at 80 K for all plots. This figure shows the distributions near the contact. The distributions over the entire channel are shown in Figure S3 in the Supporting Information.

simulated distributions of electric field, free charge carriers, and excitons at 300 K and 80 K, respectively (Figure 1). We let source-drain bias to be zero ($V_{sd} = 0\ V$) and fix the focused laser position at 10 μm away from the left contact. The laser intensity is sufficiently weak and the photoexcited electron (majority carrier) density is much lower than that in the dark, so the electronic band bending is not perturbed by the light. The electric field is only large in the Schottky junction near the contact, reaching up to 3 V/μm (Figure 1c). The electric field is slightly smaller at low temperature, likely because of the reduced effective densities of states (N_c and N_v). This electric field is on the same order of magnitude as that needed

to split excitons, which can be estimated by E_b/qa_{ex}.

The simulation allows us to visualize the distributions of free hole (minority carrier) density (p) and exciton density (n_{ex}). Both are peaked at the laser excitation position and decay much more slowly at low temperature, indicating more efficient diffusion (Figure 1d,e). Both p and n_{ex} drop to zero at the contact as enforced by the boundary condition of an infinite recombination rate. Since the photoexcited free hole density is much larger than the dark hole density ($\Delta p >> p_0$) as in the experimental condition, the free hole density is almost all from photoexcitation ($p \approx \Delta p$). We can then use the ratio $f_{ex} = n_{ex}/(n_{ex}+p)$ to evaluate the fraction of excitons over the total photoexcited carriers. f_{ex} ranges from 0 to 1 where 1 means that photoexcitation only produces excitons. Though both p and n_{ex} change significantly in the channel, the distribution of f_{ex} is uniform in the electric field free zone (Figure 1f). This is because coexisting excitons and free carriers reach a dynamical balance governed by Equation 13. This balance is not affected by the diffusion and recombination of photoexcited carriers, as both the formation and dissociation rates of excitons are much faster than the diffusion and recombination processes, as confirmed by simulation (Figures S4 and S5 in the Supporting Information). We also note that the exciton formation rate is estimated by the classical Langevin recombination (Equation 1) in this work. A more rigorous treatment that considers phonon interactions yields a similar or slightly slower exciton formation rate up to tens of ps.[37] This is still much faster than the carrier recombination and transport process and hence our conclusion that excitons and free carriers reach a balance still holds. In the field free region, f_{ex} increases from 1% at 300 K to 9% at 80 K. The reduced f_{ex} in the depletion region is caused by the exciton splitting under the strong electric field.

Temperature dependent photocurrent profiles. Next, we simulate photocurrent as a function of the photoexcitation position at $V_{sd} = 0$ V and across various temperatures. Photocurrent decays rapidly as the photoexcitation position moves away from the contact in the high-temperature phase with $E_b = 10$ meV. Below the transition temperature ($T_c =$ 160 K) when E_b becomes bigger, the decay is much slower (Figure 2a,b). Above T_c, the

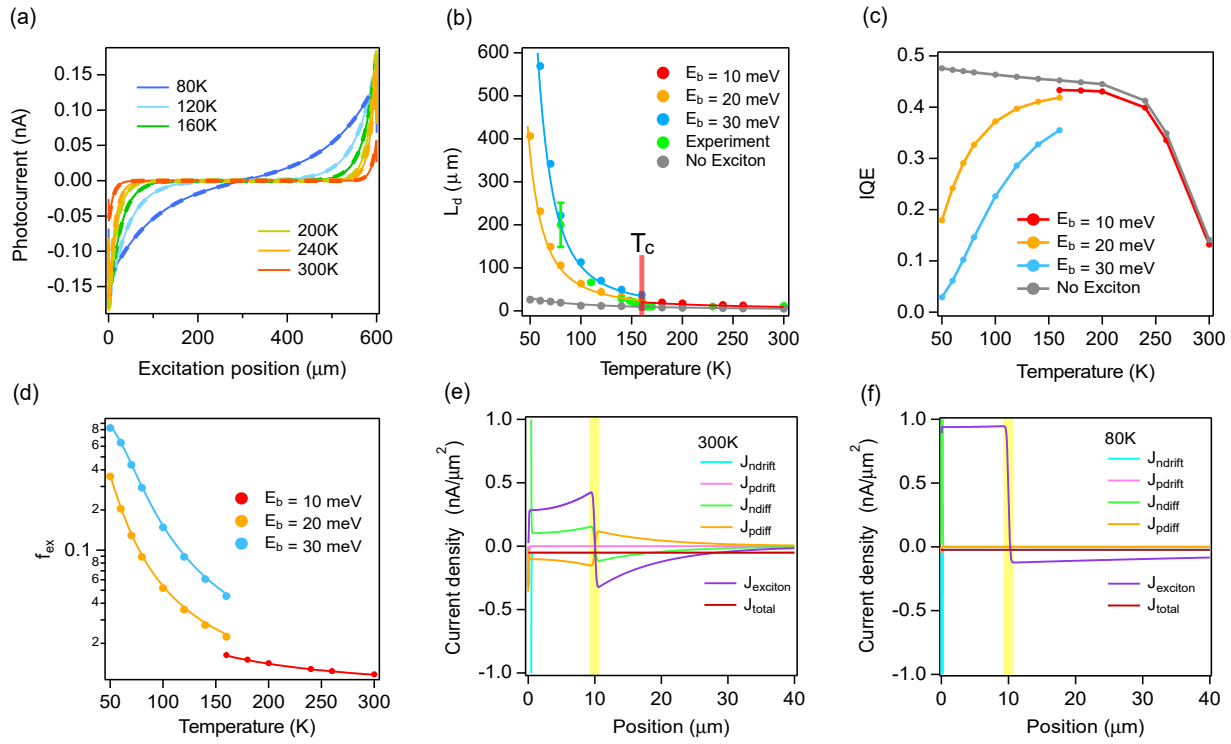

Figure 2: Simulated temperature dependent photocurrent distributions in a $MAPbI_3$ microribbon device. (a) Photocurrent as a function of the photoexcitation location at various temperatures using $E_b = 20$ meV below T_c and $E_b = 10$ meV above T_c. The solid lines are simulated values and the dashed lines are the fitting by a hyperbolic function. (b) Temperature dependent L_d at different E_b values or in the absence of excitons. The circles are L_d values extracted from the hyperbolic fitting of photocurrent distributions as in (a). The solid curves are calculated using Equation 17. The experimental results (green circles, extracted from reference[16]) are also shown to compare with the simulation. Semi-log plot is shown in Figure S6 in the Supporting Information. (c) IQE at the photocurrent peak as a function of T. (d) f_{ex} in the electric field free region as a function of T. The circles are extracted from the simulation and the solid curves are calculated using Equation 13. (e, f) Distributions of current density components at 300 K (e) and 80 K (f). The vertical yellow lines indicate the photoexcitation positions.

photocurrent decay follows very well an exponential function, from which the decay length L_d can be extracted. L_d only slightly increases from 10 to 20 μm when T is reduced from 300 K to 160 K. The values of L_d are very close to those expected from free minority carrier diffusion, indicating exciton diffusion has a negligible contribution to photocurrent at these temperatures. This is consistent with that E_b is significantly below k_BT for the high temperature phase. L_d then jumps from 20 μm to 30 μm for $E_b = 20$ meV (40 μm

for E_b = 30 meV) as T drops below T_c (Figure 2b and Figure S6), caused by the sudden increase of E_b.

At low T, photocurrent decays slowly and its profiles substantially deviate from a single exponential function, due to the decay length becoming comparable to the channel length. In order to accurately extract the decay length, we fit the curve with a hyperbolic function $I(x_0) = A \sinh \frac{x_0 - L/2}{L_d}$, where $L = 600\ \mu m$ is the channel length, and A and L_d are fitting parameters. The photocurrent distributions can be fit very well by this function. The hyperbolic fitting can be justified by considering the continuity equation and boundary conditions (see details in the Supporting Information).

As T is reduced from 160 K to 50 K, L_d extracted from the simulated photocurrent profiles increases sharply, by 11 times for E_b = 20 meV and 25 times for E_b = 30 meV. If excitons are not considered, L_d only increases by about 3 times (Figure 2b). This comparison signals the importance of the exciton contribution to the overall carrier diffusion length. The simulated T-dependent L_d, both the sudden jump across the phase transition and the rapid increase below T_c, agree very well with our previous experimental results, which are also plotted in Figure 2b. The simulated f_{ex} is close to zero above T_c and reaches about 40% for E_b = 20 meV and 80% for E_b = 30 meV at 50 K (Figure 2d).

Remarkably, both L_d and f_{ex} are also in excellent agreement with that calculated from Equations 17 and Equation 13, respectively, as shown in Figure 3b, d (solid lines are calculated curves and circles are simulated). This indicates that the assumptions made when deriving these equations, including (1) excitons and free carriers reaching a dynamic balance across the channel and (2) neglecting the free carrier current, are reasonable. These analytic expressions not only provide a simple method to estimate the L_d and f_{ex} values, but also a clear and intuitive picture on understanding the transport of photoexcited carriers. Though excitons and free carriers are set to have very different mobilities and lifetimes, their simulated distributions (Figure 1) and photocurrent profiles (Figure 2a) clearly follow an exponential (or hyperbolic) function with only one characteristic decay length (L_d), instead

of having multiple components (such as $\sqrt{D_p\tau_p}$ and $\sqrt{D_{ex}\tau_{ex}}$). This is because free carriers and excitons convert into each other frequently through a ps pairing/dissociation process, and hence reach a pseudo-equilibrium with uniform exciton fraction along the device channel (except at the Schottky junction). As a result, the coexisting free carriers and excitons can be regarded as one species moving at the much higher exciton mobility but with a hybrid lifetime as in Equation 17.

The internal quantum efficiency (IQE), defined as the ratio of electrons collected to photons absorbed in the microribbon, is calculated at the maximum current position and plotted against T (Figure 2c). The simulated IQE first increases when T is reduced from 300 K to about 250 K and then saturates at about 40%. Such an IQE increase is caused by the channel resistance (R) decreasing at lower T. As carrier mobility is assumed to increase at lower T, R decreases, resulting in an increased IQE. This explanation is confirmed by the simulation results for a shorter channel device as shown in Figure S7 in the Supporting Information. The 40% IQE (instead of the ideal 50% for the device with two Schottky contacts) is also caused by the series channel resistance.[23] If exciton formation is not considered, the simulated IQE remains high below T_c. In this case, IQE slightly increases closer to 50% as R decreases at lower T. But when exciton formation is considered, IQE significantly decreases at lower T and drops to 18% for $E_b = 20\ meV$ and 3% for $E_b = 30\ meV$ at 50 K. This is because the equilibrium constant of exciton dissociation $K(E)$ depends on T as shown in Equations 4 and 13. $K(E)$ is reduced by more than one order of magnitude at low T as shown in Figure S8 in the Supporting Information. The reduced photocurrent efficiency at lower T is consistent with previous experimental work.[38]

To better understand the photocurrent generation, we plot the simulated distributions of individual photocurrent components when the photoexcitation is fixed at $x = 10\ \mu$m at 300 K and 80 K, respectively (Figure 2e, f). The total current is the sum of four components including electron drift, electron diffusion, hole drift, and hole diffusion. Though each component varies along the channel, the total current must be uniform because of charge continuity as

shown in the plot. In comparison, we also plot the exciton diffusion current (eJ_{ex}) as defined in Equation 12. Exciton flow does not directly generate electric current because excitons are charge neutral. But excitons can be split into electrons and holes under the electric field in the Schottky junction, where the efficient charge separation can produce photocurrent. As shown clearly in the figure, the exciton current at 80 K is much higher than that at 300 K, because more excitons are formed with increased exciton binding energy. At 80 K, the exciton current is much larger than free carrier diffusion/drift components, indicating the exciton flow dominates the photocurrent generation.

Doping dependent photocurrent profiles. To compare with the experimentally measured gate dependent L_d, we simulate photocurrent distributions with various N_d values at 80 K, as both doping and gate can change the Fermi level. If only free carriers are considered, the simulated L_d values remain about the same in a large range of N_d values (Figure 3b), inconsistent with the experimental results that L_d changes by a factor of 8 under gate (Figure 3b inset).[16] The slight increase of L_d at low N_d values is caused by the longer SRH recombination lifetime at low doping density (Equation 9). On the other hand, if excitons are considered, the simulated photocurrent decays much more slowly as N_d increases (Figure 3a, b), which is consistent with the experimental results. The simulation again agrees well with Equation 17, except at very low N_d, because the n-type assumption no longer holds at such low doping concentration. Higher N_d, and hence higher electron density, increases the probability of exciton formation, leading to a larger exciton fraction as shown in Equation 13. The larger f_{ex} is confirmed directly by simulation and agrees well with the calculation by Equation 13 (Figure 3d). The simulated peak IQE drops at higher N_d (Figure 3c), presumably because the excitons are less likely to split after reaching the contact due to larger exciton fraction and smaller contact band bending. IQE also drops at lower N_d because of a more resistive channel. We note that at high N_d values or high laser intensity, E_b may be reduced because of strong field screening.[39] This effect is not considered in our simulation.

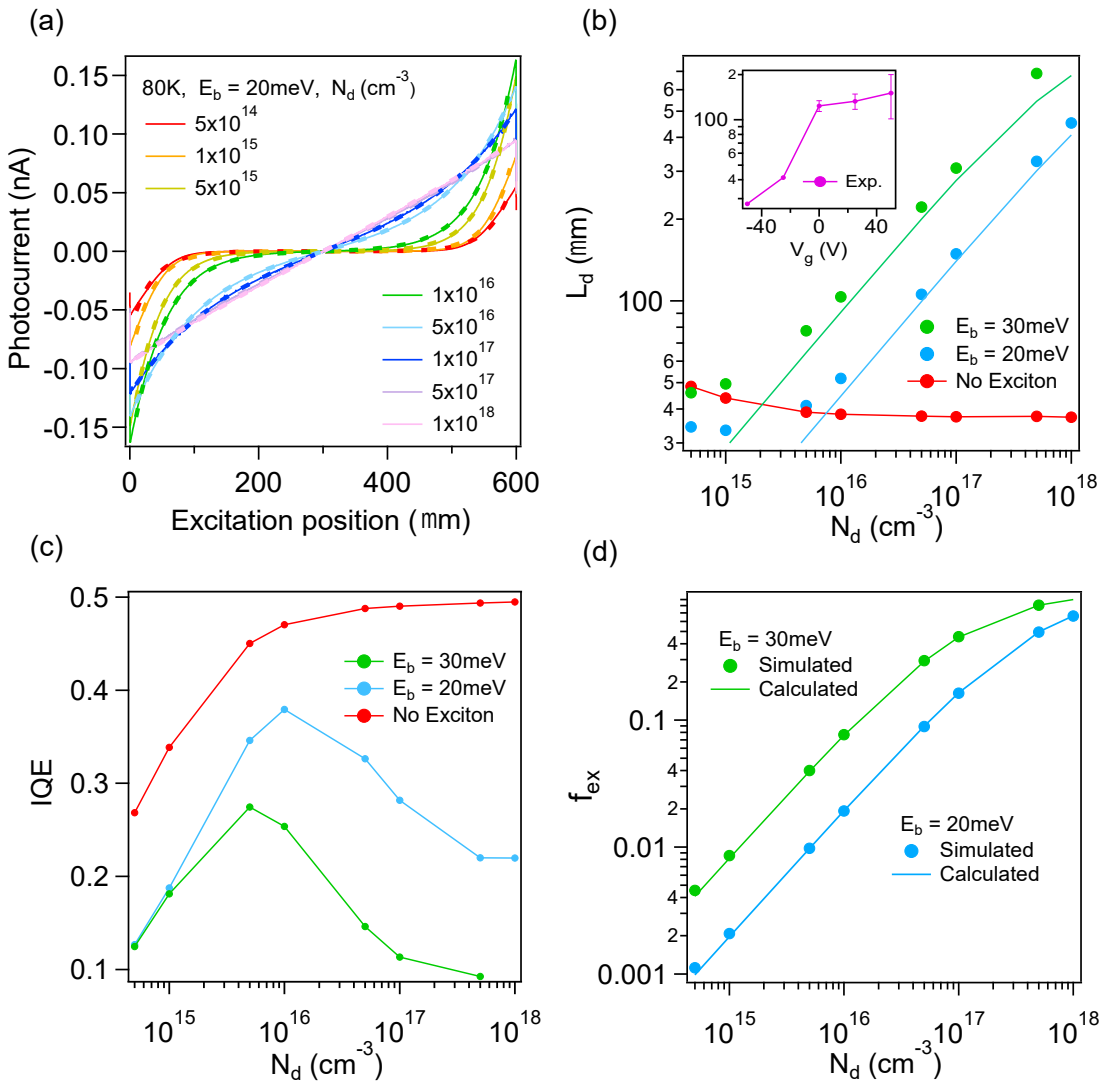

Figure 3: Simulated doping level dependent photocurrent distributions in a $MAPbI_3$ microribbon device at 80K. (a) Photocurrent as a function of the photoexcitation location with various donor concentrations for $E_b = 20$ meV below T_c. The photocurrent distributions for $E_b = 30$ meV are shown in Figure S9 in the Supporting Information. The hyperbolic fittings for extracting L_d are shown as dashed lines. (b) Donor concentration dependent L_d at different E_b values or in the absence of excitons. The circles are L_d values extracted from the hyperbolic fitting of the simulated photocurrent distributions as in (a). The solid curves are calculated using Equation 17. Inset: experimental result from reference.[16] (c) Simulated IQE at the photocurrent peak position as a function of donor concentrations. (d) Simulated exciton fraction (circles) in the electric field free zone. The expected f_{ex} values calculated by Equation 13 are shown as solid lines.

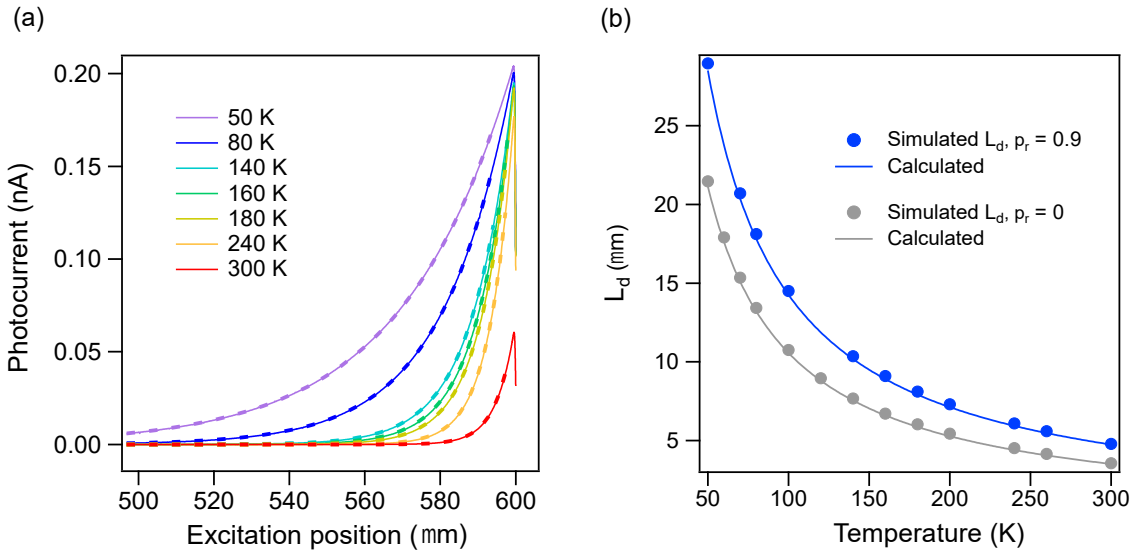

Figure 4: Simulated photocurrent distributions to take into account photon recycling effects in a $MAPbI_3$ microribbon device. (a) Simulated photocurrent profiles through a range of temperatures both below and above T_c for $p_r = 0.9$. Each curve is fitted with an exponential function, shown as a dashed line overlaying the corresponding curve. To clearly demonstrate the fitting quality, we only show the photocurrent distributions near the right contact. The left contact mirrors the right but with opposite current polarity. (b) Diffusion length L_d as a function of temperature for the baseline $p_r = 0$ (in the absence of photon recycling) and for $p_r = 0.9$. The circles are L_d values extracted from the hyperbolic fitting of the simulated photocurrent distributions as in (a). The solid curves are calculated using Equation 21.

Photon recycling effects. Photon recycling via re-absorption of emitted photons by the material has been proposed as a possible mechanism for extending the propagation of photoexcitation energy.[40] We now consider this effect using numerical simulation. To account for this effect, we add an internal generation term in the continuity equations (Equations 6 and 7) in addition to the external generation term by laser, similar to the previous work,[41]

$$G_{int} = k_{rad}\ n\ p\ p_r \tag{18}$$

where k_{rad} is the radiative recombination coefficient and p_r is the re-absorption probability. We take $p_r = 0.9$ and $k_{rad} = 2 \times 10^{-10} \times (T/300)^{3/2}\ cm^3/s$, which corresponds to a radiative lifetime that equals to the minority carrier lifetime used in the SRH recombination ($\tau_{rad} = \tau_p$)

at any temperature. We turn off the exciton effect by letting $k_d(E)$ and k_r be zero in Equations 6 and 7 and add a radiative recombination term. The new hole continuity equation in the steady state then becomes,

$$G_{ex} + G_{int} - k_{rad}np - R_{SRH} - \nabla \cdot \vec{J}_p = 0 \tag{19}$$

Electron continuity equation is similar but $\vec{J}_p$ is replaced by $\vec{J}_n$. The simulated photocurrent distributions when considering photon recycling effects show an increase of L_d by about 40% (Figure 4b). This result indicates that while photon recycling certainly can have an effect on modifying L_d, the major contribution to the experimentally observed much longer L_d is likely not from this effect. Equation 19 can be simplified under the reasonable assumptions that photocurrent is dominated by minority carrier diffusion and the photoexcitation intensity is low so that $n = N_d$. In the region outside of photoexcitation of a 1D channel that is free of electric field, the equation becomes,

$$D_p \frac{d^2p}{dx^2} = [1/\tau_p + (1 - p_r)/\tau_{rad}]p \tag{20}$$

This leads to an exponential photocurrent with a decay length given by,

$$L_d = \sqrt{\frac{D_p}{1/\tau_p + (1 - p_r)/\tau_{rad}}} \tag{21}$$

The simulated photocurrent decay lengths are consistent with this expression as shown in Figure 4b.

In summary, we have performed rigorous finite element simulations to model transport of coexisting excitons and free carriers locally excited by a focused laser. The device modeling shows that highly mobile excitons become important and dominate the photocurrent decay profiles at low temperature in halide perovskites. Our simulations are highly consistent with our previous experimental results.[16] The main conclusions are: (1) The effective diffusion length of photogenerated carriers, as evaluated by the simulated photocurrent decay length

in SPCM, rapidly increases below the phase transition temperature (Figure 2). The simulated L_d increases much faster than expected from phonon scattering of free carriers, due to the exponentially increased fraction of highly mobile excitons at lower temperature. (2) The diffusion length increases at higher doping level as the higher majority carrier concentration promotes the formation of excitons (Figure 3). (3) The temperature and doping level dependent photocurrent decay lengths both agree quite well with the analytic result expressed in Equation 17, which is derived under the assumption that excitons and free carriers reach a dynamic balance and hence the exciton fraction remains constant through the device channel. (4) The photocurrent quantum efficiency can be tuned by temperature and doping level. The efficiency reduction at low temperature or at high doping level can be understood by the difficulty of exciton splitting. (5) The simulated photon-recycling effects based on internal re-absorption do not appear to generate sufficient increase in the decay length to explain the experimental results. Our work sets up a rigorous simulation method for understanding the role of excitons in the transport of photogenerated carriers. The simulation also provides a more accurate interpretation of the experimental results obtained from a widely used spatially resolved optoelectronic technique. We expect this modeling method to be used in a variety of materials beyond halide perovskites, such as 2D materials with large excitonic binding energy.

ASSOCIATED CONTENT

AUTHOR INFORMATION

Corresponding Authors

*E-mail: yu@physics.ucdavis.edu.

ORCID

Dong Yu: 0000-0002-8386-065X

R. T. Senger: 0000-0003-0800-1924

Notes

The authors declare that they have no competing financial interests.

ACKNOWLEDGEMENT

This work was supported by the U.S. National Science Foundation Grants DMR-1710737 and DMR-1838532. R.T.S. acknowledges the support from The Turkish Fulbright Commission Visiting Scholar Program.

Supporting Information

Supporting Information Available: Analytic justification of extraction of carrier diffusion length by hyperbolic fittings; comparison of simulation results by Python and COMSOL; comparison of simulation results by initial generation of excitons or free carriers; simulated photocurrent decay lengths with temperature independent lifetimes; simulated distributions of electric field, free electron, hole, and exciton densities across the entire channel; comparison of rates for the exciton pairing, dissociation, transport, and recombination processes at 80 K and 300 K; semi-log plot of simulated photocurrent decay length as a function of temperature; simulated peak internal quantum efficiency in a shorter channel device; equilibrium constant of exciton dissociation $K(E)$ as a function of temperature; photocurrent distributions at various doping levels simulated by using excitonic binding energy of 30 meV.

References

(1) You, Y.; Zhang, X.-X.; Berkelbach, T. C.; Hybertsen, M. S.; Reichman, D. R.; Heinz, T. F. Observation of biexcitons in monolayer WSe 2. *Nat. Phys.* **2015**, *11*, 477–481.

(2) Makarov, N. S.; Guo, S.; Isaienko, O.; Liu, W.; Robel, I.; Klimov, V. I. Spectral and dynamical properties of single excitons, biexcitons, and trions in cesium–lead-halide perovskite quantum dots. *Nano Lett.* **2016**, *16*, 2349–2362.

(3) Neukirch, A. J.; Nie, W.; Blancon, J.-C.; Appavoo, K.; Tsai, H.; Sfeir, M. Y.; Katan, C.; Pedesseau, L.; Even, J.; Crochet, J. J. et al. Polaron stabilization by cooperative lattice distortion and cation rotations in hybrid perovskite materials. *Nano Lett.* **2016**, *16*, 3809–3816.

(4) Su, R.; Diederichs, C.; Wang, J.; Liew, T. C.; Zhao, J.; Liu, S.; Xu, W.; Chen, Z.; Xiong, Q. Room-temperature polariton lasing in all-inorganic perovskite nanoplatelets. *Nano Lett.* **2017**, *17*, 3982–3988.

(5) Stern, M.; Umansky, V.; Bar-Joseph, I. Exciton liquid in coupled quantum wells. *Science* **2014**, *343*, 55–57.

(6) High, A. A.; Leonard, J. R.; Hammack, A. T.; Fogler, M. M.; Butov, L. V.; Kavokin, A. V.; Campman, K. L.; Gossard, A. C. Spontaneous coherence in a cold exciton gas. *Nature* **2012**, *483*, 584–588.

(7) Hou, Y.; Wang, R.; Xiao, R.; McClintock, L.; Travaglini, H. C.; Francia, J. P.; Fetsch, H.; Erten, O.; Savrasov, S. Y.; Wang, B. et al. Millimetre-long transport of photogenerated carriers in topological insulators. *Nat. Commun.* **2019**, *10*, 1–7.

(8) Williams, R.; Song, K. The self-trapped exciton. *J. Phys. Chem. Solids* **1990**, *51*, 679–716.

(9) Yuan, Z.; Zhou, C.; Tian, Y.; Shu, Y.; Messier, J.; Wang, J. C.; Van De Burgt, L. J.; Kountouriotis, K.; Xin, Y.; Holt, E. et al. One-dimensional organic lead halide perovskites with efficient bluish white-light emission. *Nat. Commun.* **2017**, *8*, 14051.

(10) Tamor, M.; Wolfe, J. Drift and diffusion of free excitons in Si. *Phys. Rev. Lett.* **1980**, *44*, 1703.

(11) Rakita, Y.; Cohen, S. R.; Kedem, N. K.; Hodes, G.; Cahen, D. Mechanical properties of APbX 3 (A= Cs or CH 3 NH 3; X= I or Br) perovskite single crystals. *MRS. Commun.* **2015**, *5*, 623–629.

(12) Sendner, M.; Nayak, P. K.; Egger, D. A.; Beck, S.; Müller, C.; Epding, B.; Kowalsky, W.; Kronik, L.; Snaith, H. J.; Pucci, A. et al. Optical phonons in methylammonium lead halide perovskites and implications for charge transport. *Mater. Horiz.* **2016**, *3*, 613–620.

(13) Devreese, J. T.; Alexandrov, A. S. Fröhlich polaron and bipolaron: recent developments. *Rep. Prog. Phys* **2009**, *72*, 066501.

(14) Miyata, K.; Atallah, T. L.; Zhu, X.-Y. Lead halide perovskites: Crystal-liquid duality, phonon glass electron crystals, and large polaron formation. *Sci. Adv.* **2017**, *3*, e1701469.

(15) Wright, A. D.; Verdi, C.; Milot, R. L.; Eperon, G. E.; Pérez-Osorio, M. A.; Snaith, H. J.; Giustino, F.; Johnston, M. B.; Herz, L. M. Electron–phonon coupling in hybrid lead halide perovskites. *Nat. Commun.* **2016**, *7*, 1–9.

(16) McClintock, L.; Xiao, R.; Hou, Y.; Gibson, C.; Travaglini, H. C.; Abramovitch, D.; Tan, L. Z.; Senger, R. T.; Fu, Y.; Jin, S. et al. Temperature and gate dependence of carrier diffusion in single crystal methylammonium lead iodide perovskite microstructures. *J. Phys. Chem. Lett.* **2020**, *11*, 1000–1006.

(17) Merzbacher, E. *Quantum Mechanics*, 3rd ed.; John Wiley Sons, Inc.: New York, 1998; p 462.

(18) Pollmann, J.; Büttner, H. Effective Hamiltonians and binding energies of Wannier excitons in polar semiconductors. *Phys. Rev. B* **1977**, *16*, 4480–4490.

(19) Senger, R. T.; Bajaj, K. K. Optical properties of confined polaronic excitons in spherical ionic quantum dots. *Phys. Rev. B* **2003**, *68*, 045313.

(20) D'innocenzo, V.; Grancini, G.; Alcocer, M. J.; Kandada, A. R. S.; Stranks, S. D.; Lee, M. M.; Lanzani, G.; Snaith, H. J.; Petrozza, A. Excitons versus free charges in organo-lead tri-halide perovskites. *Nat. Commun.* **2014**, *5*, 3586.

(21) Häusermann, R.; Knapp, E.; Moos, M.; Reinke, N. A.; Flatz, T.; Ruhstaller, B. Coupled optoelectronic simulation of organic bulk-heterojunction solar cells: Parameter extraction and sensitivity analysis. *J. Appl. Phys.* **2009**, *106*, 104507.

(22) Graham, R.; Yu, D. Scanning photocurrent microscopy in semiconductor nanostructures. *Mod. Phys. Lett. B* **2013**, *27*, 1330018.

(23) Xiao, R.; Hou, Y.; Law, M.; Yu, D. On the use of photocurrent imaging to determine carrier diffusion lengths in nanostructured thin-film field-effect transistors. *J. Phys. Chem. C* **2018**, *122*, 18356–18364.

(24) Fu, D.; Zou, J.; Wang, K.; Zhang, R.; Yu, D.; Wu, J. Electrothermal dynamics of semiconductor nanowires under local carrier modulation. *Nano Lett.* **2011**, *11*, 3809–3815.

(25) Xiao, R.; Hou, Y.; Fu, Y.; Peng, X.; Wang, Q.; Gonzalez, E.; Jin, S.; Yu, D. Photocurrent mapping in single-crystal methylammonium lead iodide perovskite nanostructures. *Nano Lett.* **2016**, *16*, 7710–7717.

(26) Semonin, O. E.; Elbaz, G. A.; Straus, D. B.; Hull, T. D.; Paley, D. W.; Van der Zande, A. M.; Hone, J. C.; Kymissis, I.; Kagan, C. R.; Roy, X. et al. Limits of carrier diffusion in N-type and P-type CH3NH3PbI3 perovskite single crystals. *J. Phys. Chem. Lett.* **2016**, *7*, 3510–3518.

(27) Wang, X.; Ling, Y.; Chiu, Y.-C.; Du, Y.; Barreda, J. L.; Perez-Orive, F.; Ma, B.; Xiong, P.; Gao, H. Dynamic electronic junctions in organic–inorganic hybrid perovskites. *Nano Lett.* **2017**, *17*, 4831–4839.

(28) Braun, C. L. Electric field assisted dissociation of charge transfer states as a mechanism of photocarrier production. *J. Chem. Phys.* **1984**, *80*, 4157–4161.

(29) Fuoss, R.; Accascina, F. *Electrolytic conductance*; Interscience Publishers, 1959.

(30) Kulig, M.; Zipfel, J.; Nagler, P.; Blanter, S.; Schüller, C.; Korn, T.; Paradiso, N.; Glazov, M. M.; Chernikov, A. Exciton diffusion and halo effects in monolayer semiconductors. *Phys. Rev. Lett.* **2018**, *120*, 207401.

(31) Saha, M. N. On a physical theory of stellar spectra. *Proc. R. Soc. London, Ser. A* **1921**, *99*, 135–153.

(32) Mariano, F.; Cretì, A.; Carbone, L.; Genco, A.; D'Agostino, S.; Carallo, S.; Montagna, G.; Lomascolo, M.; Mazzeo, M. The enhancement of excitonic emission crossing Saha equilibrium in trap passivated CH3NH3PbBr3 perovskite. *Commun. Phys.* **2020**, *3*, 1–10.

(33) Baranowski, M.; Plochocka, P. Excitons in Metal-Halide Perovskites. *Adv. Energy Mater.* **2020**, *10*, 1903659.

(34) Jiang, Y.; Wang, X.; Pan, A. Properties of excitons and photogenerated charge carriers in metal halide perovskites. *Adv. Mater.* **2019**, *31*, 1806671.

(35) Frost, J. M. Calculating polaron mobility in halide perovskites. *Phys. Rev. B* **2017**, *96*, 195202.

(36) Schenk, A. A model for the field and temperature dependence of Shockley-Read-Hall lifetimes in silicon. *Solid-State Electron.* **1992**, *35*, 1585–1596.

(37) Piermarocchi, C.; Tassone, F.; Savona, V.; Quattropani, A.; Schwendimann, P. Exciton formation rates in GaAs/Al x Ga 1- x As quantum wells. *Phys. Rev. B* **1997**, *55*, 1333.

(38) Phuong, L. Q.; Nakaike, Y.; Wakamiya, A.; Kanemitsu, Y. Free excitons and exciton–phonon coupling in CH3NH3PbI3 single crystals revealed by photocurrent and photoluminescence measurements at low temperatures. *J. Phys. Chem. Lett.* **2016**, *7*, 4905–4910.

(39) Feneberg, M.; Osterburg, S.; Lange, K.; Lidig, C.; Garke, B.; Goldhahn, R.; Richter, E.; Netzel, C.; Neumann, M. D.; Esser, N. et al. Band gap renormalization and Burstein-Moss effect in silicon-and germanium-doped wurtzite GaN up to 10^{20} cm^{-3}. *Phys. Rev. B* **2014**, *90*, 075203.

(40) Pazos-Outón, L. M.; Szumilo, M.; Lamboll, R.; Richter, J. M.; Crespo-Quesada, M.; Abdi-Jalebi, M.; Beeson, H. J.; Vrućinić, M.; Alsari, M.; Snaith, H. J. et al. Photon recycling in lead iodide perovskite solar cells. *Science* **2016**, *351*, 1430–1433.

(41) Kirchartz, T.; Márquez, J. A.; Stolterfoht, M.; Unold, T. Photoluminescence-based characterization of halide perovskites for photovoltaics. *Adv. Energy Mater.* **2020**, *10*, 1904134.